SYNRAD3D PHOTON PROPAGATION AND SCATTERING SIMULATIONS*

G. Dugan, D. Sagan,
CLASSE, Cornell University, Ithaca, NY, US

INTRODUCTION

The Bmad software library [1] has been used very successfully at Cornell for modeling relativistic charged particles in storage rings and linacs. Associated with this library are a number of programs used for lattice design and analysis. Recently, as part of the CESRTA program [2], a new program that uses the Bmad library, called `Synrad3D` [3, 4], has been developed to track synchrotron radiation photons generated in storage rings and linacs.

The motivation for developing `Synrad3D` was to estimate the energy and position distribution of photon absorption sites, which are critical inputs to codes which model the growth of electron clouds. `Synrad3D` includes scattering from the vacuum chamber walls, based on X-ray data from an LBNL database [5] for the smooth-surface reflectivity, and an analytical model [6, 7] for diffuse scattering from a surface with finite roughness. `Synrad3D` can handle any planar lattice and a wide variety of vacuum chamber profiles.

In the following sections, the general approach used in `Synrad3D` will be described. The models used for the vacuum chamber, for specular reflection, and for diffuse reflection, will be described. Examples of the application to the program to predict the radiation environment in the CESRTA ring will be presented. Comparison of the scattering model with X-ray data from DAΦNE will be given. Finally, an application of the program to predict the radiation environment in the ILC damping ring will be shown.

GENERAL APPROACH

`Synrad3D` uses Monte Carlo techniques to generate simulated photons based on the standard synchrotron radiation formulas for charged beam particles traversing dipoles, quadrupoles and wigglers, in the lattice of an accelerator. Any planar lattice can be handled. The lattice can be specified using Bmad, MAD, or XSIF format [8].

Photons are generated with respect to the particle beam's closed orbit, so the effect of variations in the orbit can be studied. In a linear accelerator lattice, since there is no closed orbit, the orbit is calculated from the user supplied initial orbit. The particle beam size is also taken into account when generating the photon starting positions. The emittance needed to calculate the beam size can be supplied by the user or is calculated from the standard synchrotron radiation formulas.

* Work supported by the US National Science Foundation (PHY-0734867, PHY-1002467, and PHY-1068662), and US Department of Energy

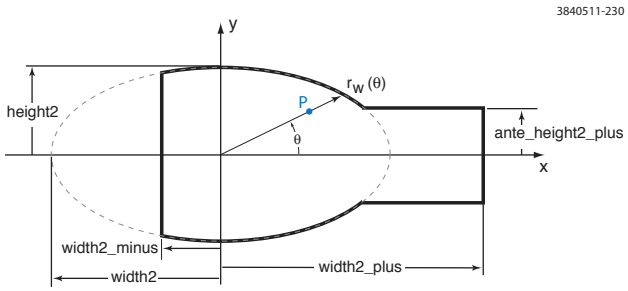

Figure 1: Vacuum chamber model

VACUUM CHAMBER MODEL

The vacuum chamber wall is characterized at a number of longitudinal positions by its cross-section. The cross section model is shown in Fig. 1. As shown in the figure, antechambers can be included.

A vacuum chamber wall cross-section may also be characterized as a general shape, by specifying points and connecting them with elliptical or linear segments.

In between the cross-sections, linear interpolation or triangular meshing can be used. Linear interpolation is faster but is best suited for convex chamber shapes. If triangular meshing is used, the segments connecting the points defining a general shape must be linear.

SCATTERING MODEL

Simulated photons are tracked until they hit the vacuum chamber wall, where the probability of being scattered, and the scattering angle, are determined by their energy and angle of incidence. This section describes the scattering model.

Specular reflection

The smooth-surface reflectivity characterizes the probability of specular reflection when a photon strikes the wall. This reflectivity is a function of the incident angle, the photon energy, and the material properties of the surface. The reflectivity is entered into the program in the form of a table. The smooth-surface reflectivity model for a technical aluminum surface (a 10 nm carbon film on an aluminum substrate), which is current default in the program, is illustrated in Fig. 2. It has been taken from an LBNL X-ray scattering database[5].

In the following subsections, we present four examples of `Synrad3D` photon production, transport and absorption simulations using CESRTA lattices and vacuum chambers. All scattering is specular only in these examples.

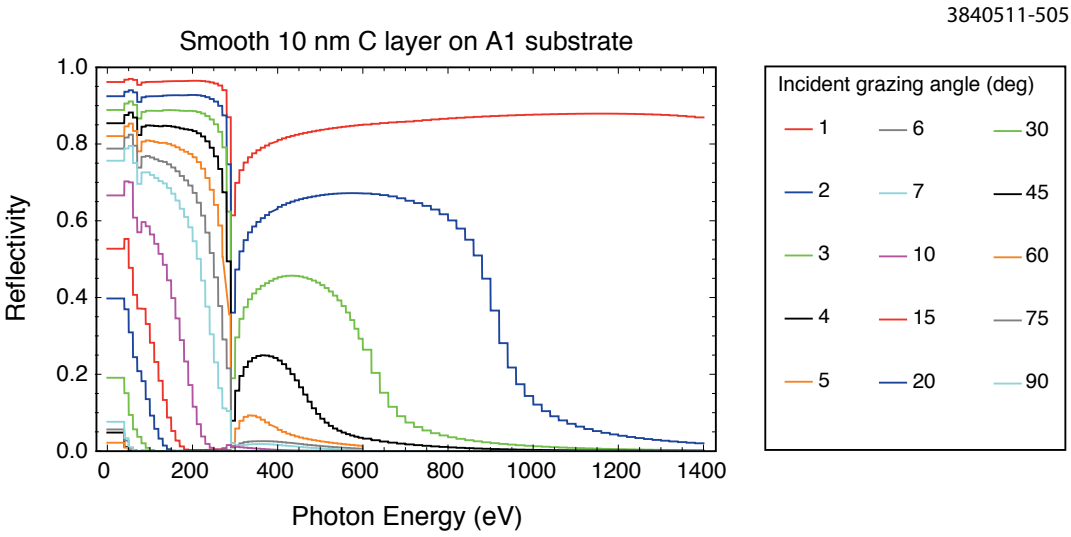

Figure 2: Smooth surface reflectivity for a 10 nm C film on Al substrate: from [5]

Example S1: Photon Emission in a Dipole As the first example, we consider the CESRTA ring with a 5.3 GeV positron beam, and use `Synrad3D` to simulate photon emission only in one arc dipole. The vacuum chamber is a simple ellipse (dimensions 9 cm horizontal by 5 cm vertical).The photons are generated only in the upstream end of the dipole but propagate downstream and can scatter.

In Fig. 3, we show a collection of photon trajectories, projected onto the bend plane. Photons generated by the beam strike the dipole vacuum chamber a short distance downstream. Some are absorbed here, but most scatter and strike the vacuum chamber further downstream, in the next

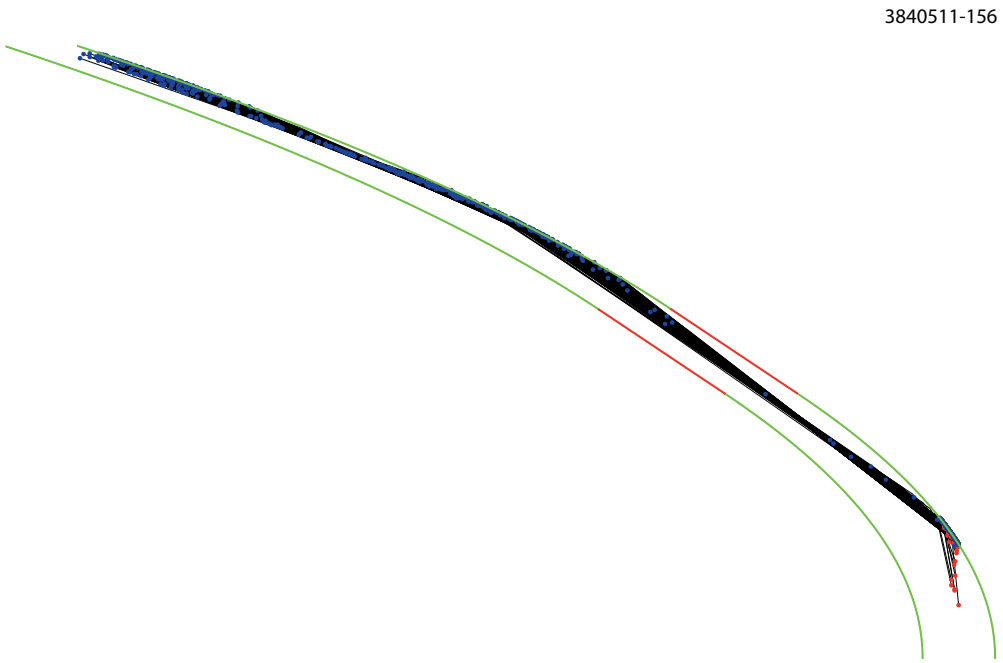

Figure 3: Projections onto the bend plane of photon trajectories from radiation in a dipole. The red dots at the lower right are the photon source (the radiating beam in a section of the dipole). Black lines are projected photon trajectories, and blue dots are photon absorption sites. The green lines in the lower right are the edges of the vacuum chamber in the dipole; the red lines are the edges in a straight section, and the green lines on the left are the edges of the vacuum chamber in the next dipole. The geometry has been distorted for purposes of illustration.

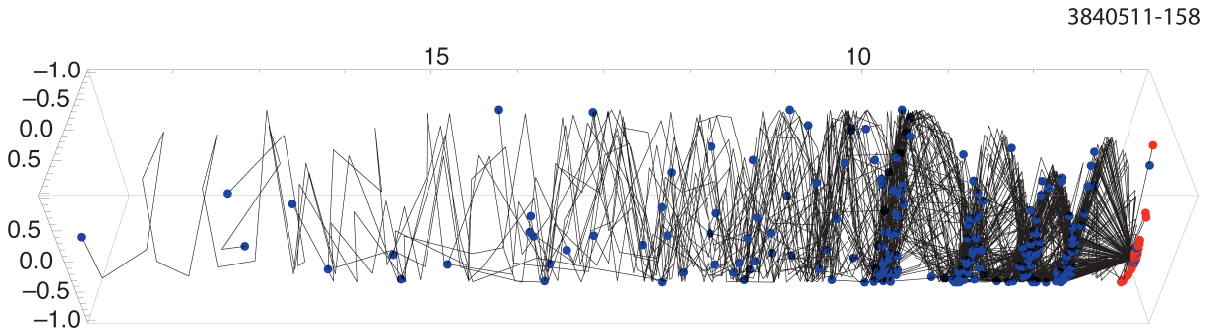

Figure 4: Photon trajectories from a dipole in three dimensions. The photon source is on the right. Black lines are trajectories, and blue dots are photon absorption sites. The transverse geometry has been distorted from an ellipse to a circle, and the longitudinal dimension has been rectified and divided by 10, for purposes of illustration.

dipole. More are absorbed here, but many others scatter again.

To emphasize the three-dimensional nature of the simulation, these photon trajectories in three dimensions are shown in Fig. 4. Photons from the source (on the right) propagate and strike the vacuum chamber. Blue dots represent absorption sites. For this simple example, in which the photon source is localized longitudinally, the absorption site locations tend to be clumped in several clusters (at the location of downstream dipoles), with decreasing intensity as we get further from the source.

Other features of the photon scattering and absorption process are shown in Fig. 5 and Fig. 6.

In Fig. 5 (left), a histogram of the number of reflections is presented. Many photons suffer no reflections, that is, they are absorbed as soon as they hit the vacuum chamber, but most are reflected several times before being absorbed. The mean number of reflections is 5.4.

In Fig. 5 (right), a histogram of the energy of all absorbed photons is presented. This is strongly peaked at zero but has a long tail out to several keV.

In Fig. 6, a two dimensional histogram of the number of photons vs. location of the absorption site along the vacuum chamber perimeter is presented. This is is peaked at the outside edge of the vacuum chamber, where the direct photon strikes occur, but there is long tail extending around the entire surface of the vacuum chamber, due to the reflected photons.

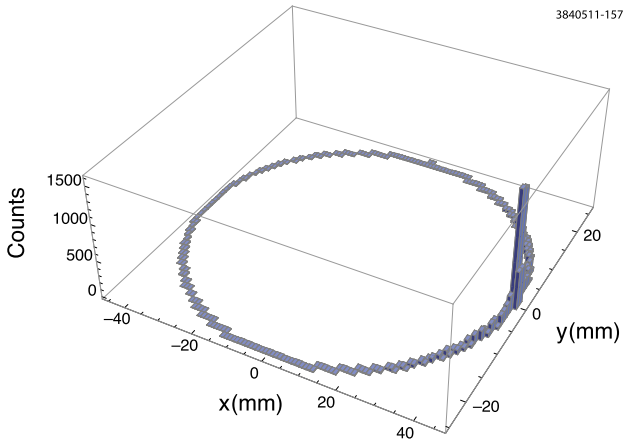

Figure 6: Distribution of photon absorption sites around the vacuum chamber perimeter

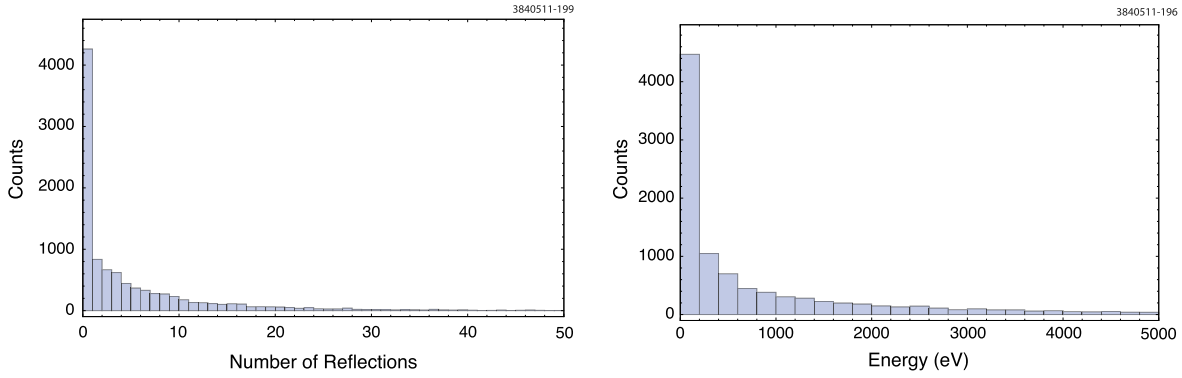

Figure 5: Reflection distribution (left) and energy distribution (right). The mean number of reflections is 5.1

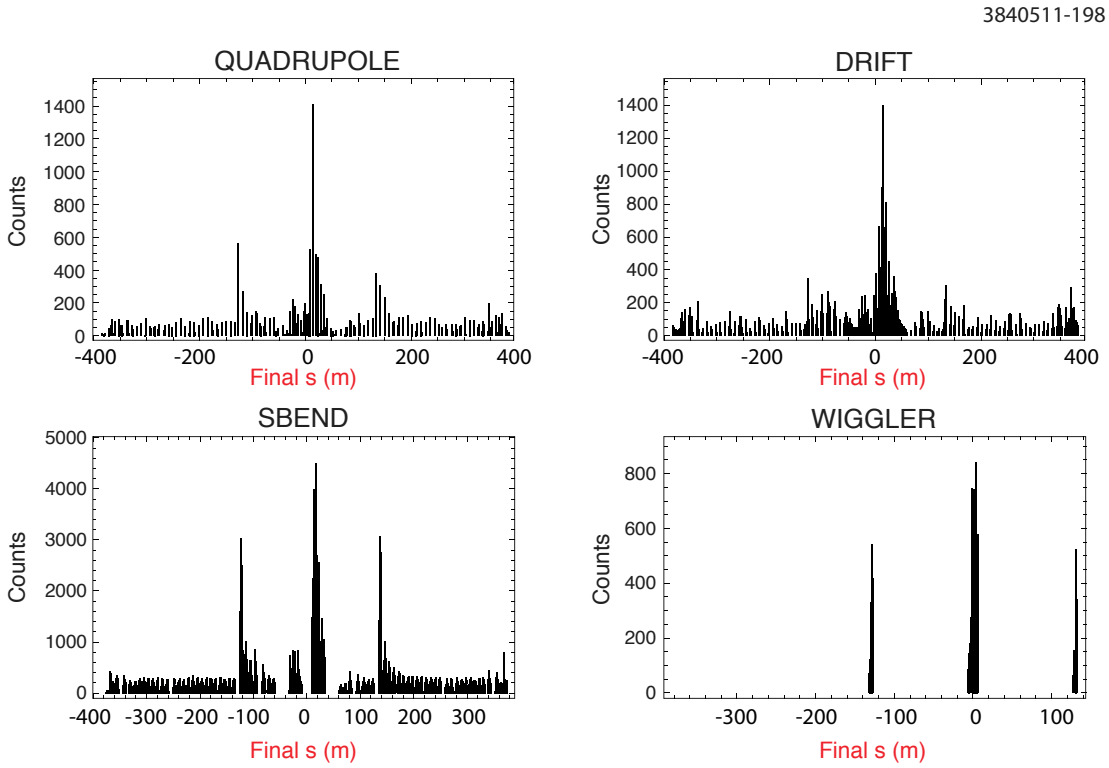

Figure 7: Distribution of photon absorption sites vs. longitudinal position, for different magnetic environments. The origin for the longitudinal coordinate is the center of the L0 straight section. The ring circumference is about 760 m.

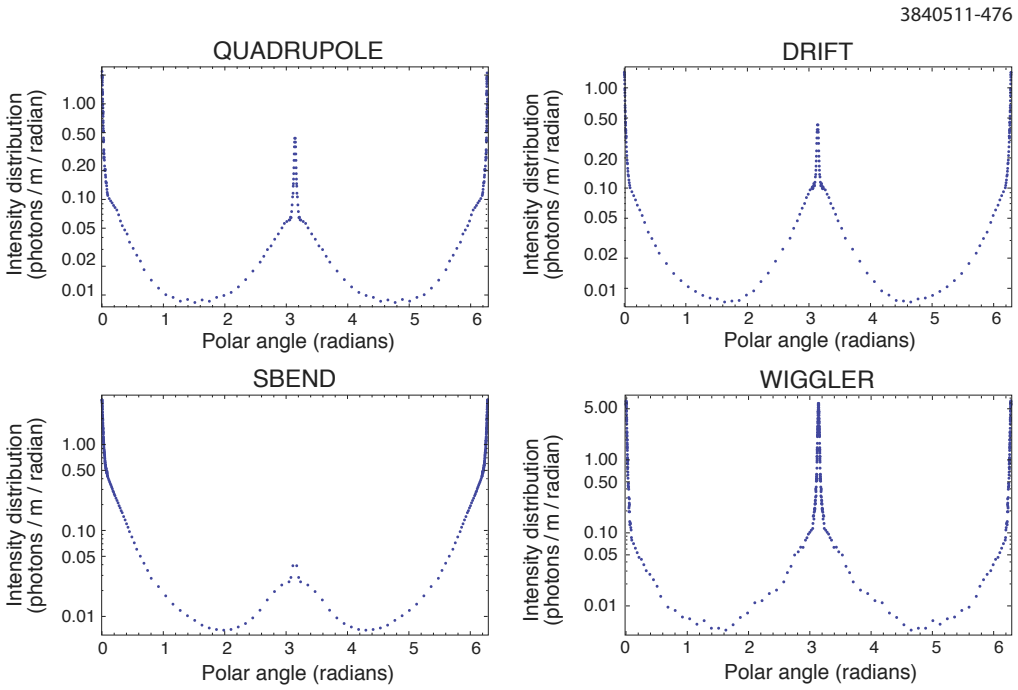

Figure 8: Photon intensity distribution (in photons/meter/radian) vs. polar angle (measured around the vacuum chamber, with zero angle corresponding to the radial outside direction), averaged over each type of magnetic environment. A 9 cm (horizontal) by 5 cm (vertical) elliptical vacuum chamber profile is assumed throughout the ring, and all scattering is specular. Top-bottom symmetry is assumed.

Example S2: Photon emission throughout the ring, elliptical vacuum chamber, no diffuse scattering For the second example, photon emission throughout the CESRTA ring from a 2.1 GeV positron beam is simulated. (The lattice name is `2085mev_20090516`). The vacuum chamber is again a simple ellipse, and the scattering is purely specular.

In Fig. 7, the distribution of photon absorption sites around the ring is shown, sorted by the type of magnetic environment in which the absorption occurs. This information is important for simulations of electron cloud growth, which is strongly influenced by the magnetic environment.

The wigglers in the L0 straight section are responsible for the large peaks near $s = 0$. The large peaks near $s = \pm 130$ m are due to wigglers in the arcs near these locations. The small peaks in the arcs are due to the regular CESRTA dipoles.

In Fig. 8, we present the photon intensity distribution (in photons/meter/radian) vs. polar angle (measured around the vacuum chamber, with zero angle corresponding to the radial outside direction), averaged over each type of magnetic environment.

In the wigglers, most of the photons come from the radiation fans in an upstream wiggler region, so there are strong peaks on both edges of the vacuum chamber. In the bends, most of the radiation is from direct strikes from upstream dipoles, so there is only a strong peak on the radial outside edge, together with a long tail, due to scattering. In the quadrupoles and drifts, there are two peaks, with the higher one at the radial outside. The peak on the radial inside, and the distribution between the peaks, are due to scattering.

Example S3: Photon emission throughout the ring, realistic vacuum chamber, no diffuse scattering For the third example, photon emission throughout the CESRTA ring from a 2.1 GeV positron beam is simulated again, but now with a realistic vacuum chamber profile. The scattering is purely specular, as in the previous example.

In Fig. 9, we present the photon intensity distribution (in photons/meter/radian) vs. polar angle (measured around the vacuum chamber, with zero angle corresponding to the radial outside direction), averaged over each type of magnetic environment.

Compared to the previous example, the photon intensity on the top and bottom of the chamber (polar angles of $\pi/2$ and $3\pi/2$) is substantially suppressed, while the radiation striking the radial inside edge of the vacuum chamber (polar angle near π) is enhanced. This is primarily due to the local shape of the vacuum chamber at the strike point of the direct synchrotron radiation. For the elliptical chamber, the wall is curved at the radiation strike point, which, for a finite width radiation stripe, enhances scattering out of the median plane. For the real CESRTA chamber, for most of the ring, the wall is vertical at the radiation strike point, so scattering out of the median plane is reduced.

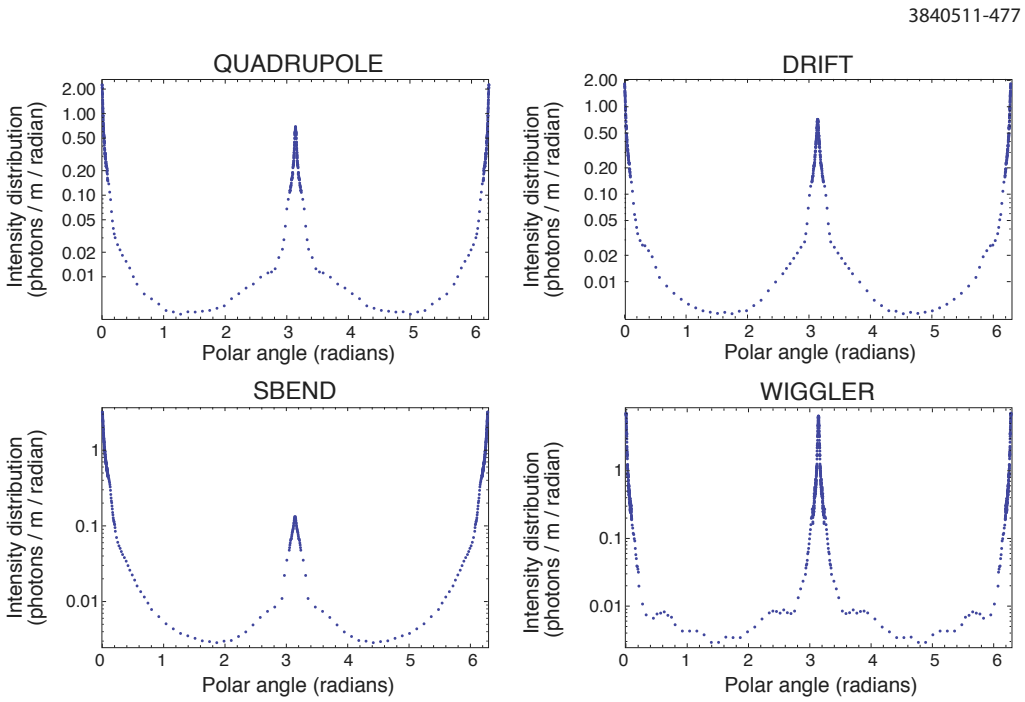

Figure 9: Photon intensity distribution (in photons/meter/radian) vs. polar angle (measured around the vacuum chamber, with zero angle corresponding to the radial outside direction), averaged over each type of magnetic environment. A realistic model for the CESRTA vacuum chamber throughout the ring is used. All scattering is specular. Top-bottom symmetry is assumed.

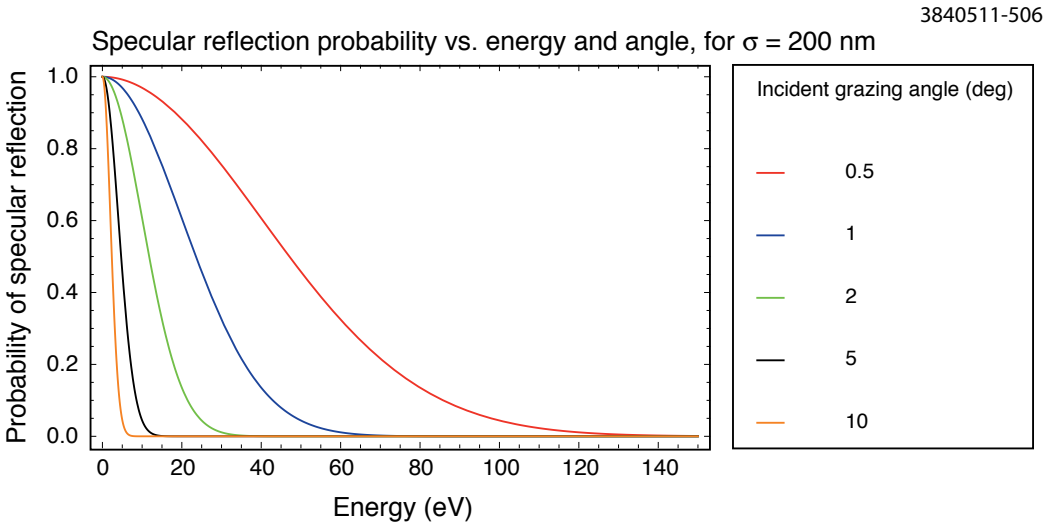

Figure 10: Specular reflection probability [6], vs. photon energy and angle, for an rms surface roughness of 200 nm.

Diffuse reflection

Generally, the probability of specular reflection of a photon from a rough surface depends on the the rms surface roughness σ, the photon wavelength λ, and the grazing angle. An explicit formula for this probability is [6]

$$P_{\text{spec}} = \mathrm{e}^{-g(x,y)}, \tag{1}$$

in which

$$g(x,y) = \frac{4\pi^2\sigma^2(x+y)^2}{\lambda^2} \tag{2}$$

where x is the cosine of the incident polar angle, and y is the cosine of the scattered polar angle. For a typical technical vacuum chamber surface, the rms surface roughness $\sigma \sim 200$ nm is greater than most of the X-ray wavelengths of interest, for all except the lowest energy photons. In this regime, except at very small grazing angles, diffuse scattering from the surface dominates over specular reflection. This is illustrated in Fig. 10.

The theory of diffuse scattering of electromagnetic waves from random rough surfaces is a well-developed subject, and is covered in detail in references [6] and [7]. The model used in `Synrad3D` is based on scalar Kirchhoff theory; this model has been used successfully to describe the scattering of soft X-rays from metal surfaces [9, 10]. In `Synrad3D`, we assume a Gaussian distribution for both the surface height variations (rms σ) and for the transverse distribution (equal in both transverse directions, with autocorrelation coefficient T).

The most general expression for the diffusely scattered power involves an infinite sum. This full expression is used in `Synrad3D`. However, the expression simplifies substantially in the limit $g(x,y) \gg 1$. This condition is satisfied for very rough surfaces, corresponding to technical vacuum chambers, and for high energy photons, for which typically $\sigma \gg \lambda$. In this limit, the diffusely scattered power per unit solid angle is given by

$$\frac{dP_{\text{diff}}}{d\Omega} = P_0 \frac{\langle R\rangle}{4\pi y}\frac{(1+xy)^2}{(x+y)^4}\times \tau^2 \mathrm{e}^{-\frac{(2-x^2-y^2)\tau^2}{4(x+y)^2}}(1-a\cos\phi)^2\mathrm{e}^{b\cos\phi}, \tag{3}$$

with

$$a = \frac{h(x,y)}{1+xy}, \tag{4}$$

$$b = \frac{2h(x,y)\tau^2}{4(x+y)^2}, \tag{5}$$

$$h(x,y) = \sqrt{1-(x^2+y^2)+x^2y^2}. \tag{6}$$

In this expression, P_0 is the incident power, $\langle R\rangle$ is the smooth-surface reflectivity, and ϕ is the scattering angle out of the plane of incidence. Note that the relative power depends on the ratio $\tau = T/\sigma$, and not on T or σ separately.

The smooth-surface reflectivity $\langle R\rangle$ depends on the atomic structure of the surface materials (including any thin layers which may be deposited on the surface). The surface roughness parameters σ and T depend on the geometry of the surface deviations from a perfect plane. These parameters may be determined from inspection of the vacuum chamber surface, for example, using an atomic force microscope.

Diffuse scattering distributions for 30 eV photons are shown in Fig. 11 and Fig. 12. At this low photon energy, the approximation $g(x,y) \gg 1$ does not hold in general, and the full diffuse scattering formalism is used to compute these distributions. Diffuse scattering distributions for high energy photons, for which $g(x,y) \gg 1$ are shown in Fig. 13 and Fig. 14. These distributions have been computed from Eq. 3.

In the following subsections, we present two examples of `Synrad3D` photon production, transport and absorption

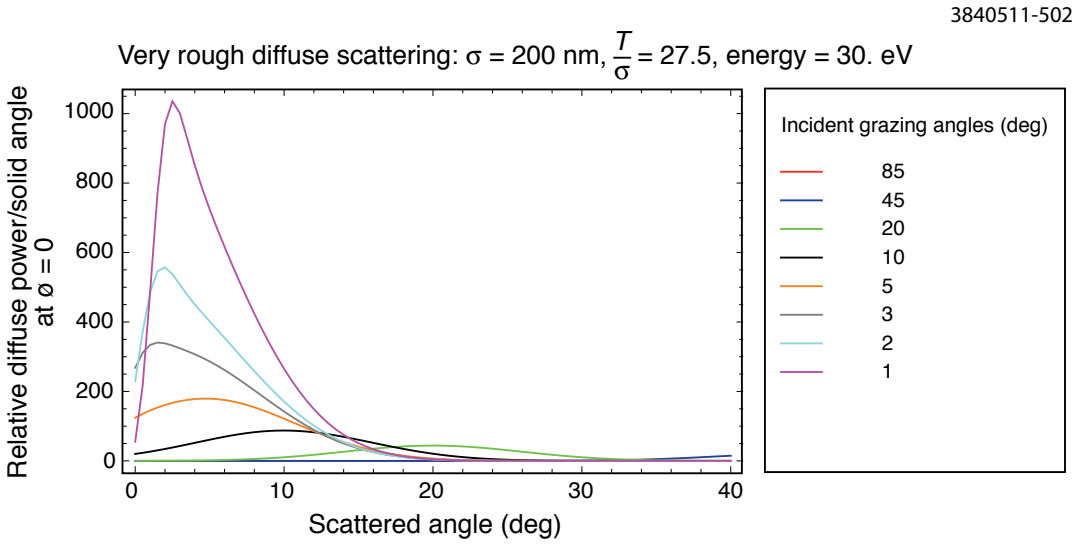

Figure 11: Diffuse scattering polar angular distributions for 30 eV photons. The full diffuse scattering expression has been used to calculate these curves.

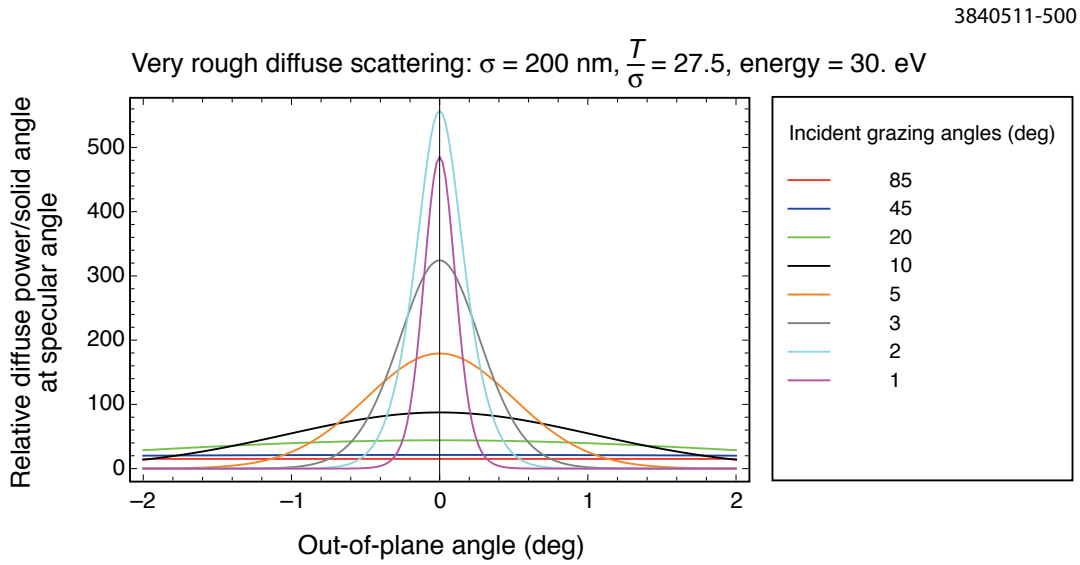

Figure 12: Diffuse scattering out-of-plane angular distributions for 30 eV photons. The full diffuse scattering expression has been used to calculate these curves.

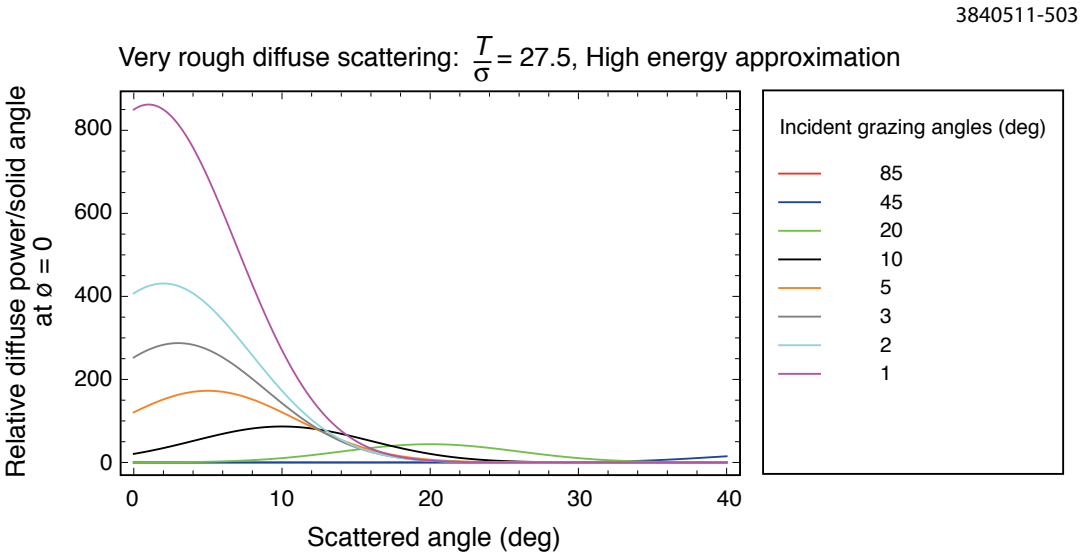

Figure 13: Diffuse scattering polar angular distributions for high energy photons. The curves are calculated from the approximate relation given in Eq. 3.

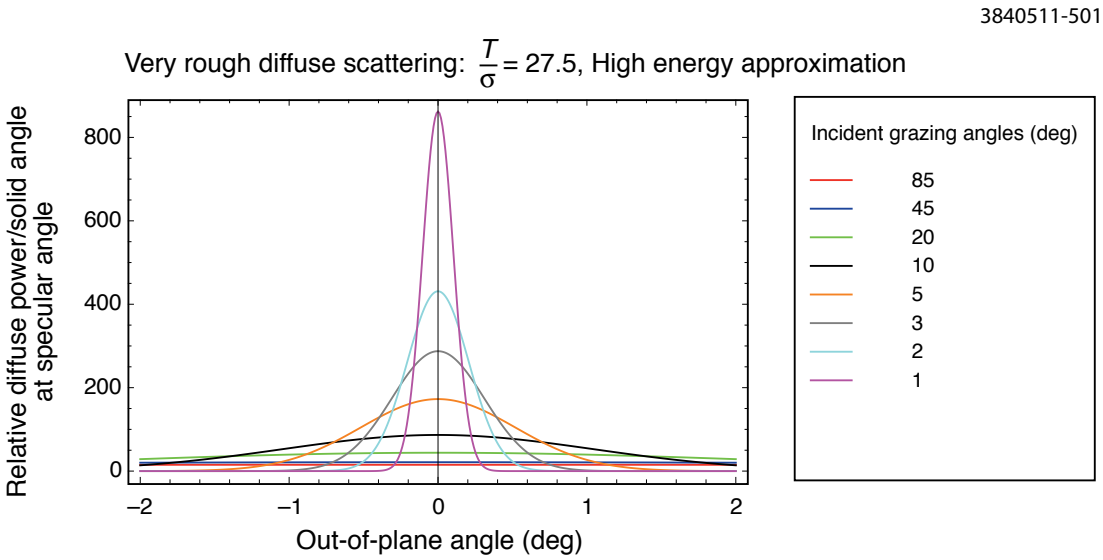

Figure 14: Diffuse scattering out-of-plane angular distributions for high energy photons. The curves are calculated from the approximate relation given in Eq. 3.

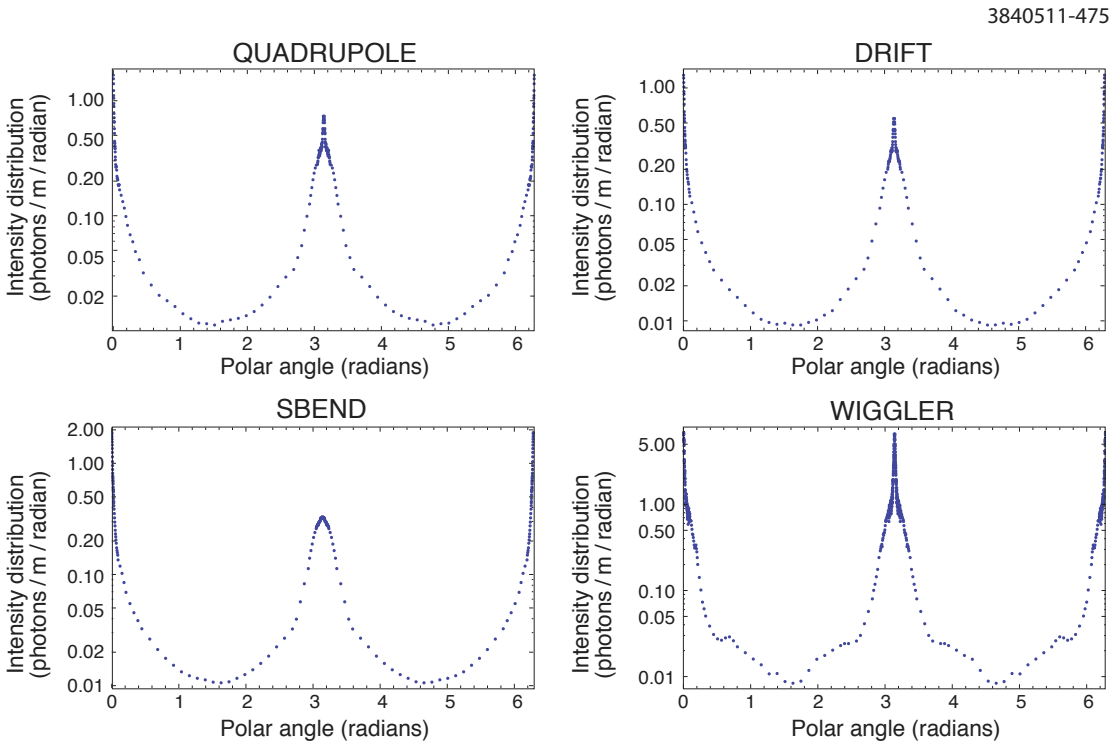

Figure 15: Photon intensity distribution (in photons/meter/radian) vs. polar angle (measured around the vacuum chamber, with zero angle corresponding to the radial outside direction), averaged over each type of magnetic environment. A realistic model for the CESR vacuum chamber throughout the ring is used, and diffuse scattering is included. Top-bottom symmetry is assumed.

simulations using CESRTA lattices and vacuum chambers, in which diffuse scattering is included in the simulation.

Example D1: Photon emission throughout the ring, realistic vacuum chamber, diffuse scattering included. For the first example, photon emission throughout the CESRTA ring from a 2.1 GeV positron beam is simulated again, with a realistic vacuum chamber profile. In this case, diffuse scattering is included, using the model described in the previous section. The surface roughness parameters used in the simulation were $\sigma = 100$ nm and $T = 5000$ nm.

In Fig. 15, we present the photon intensity distribution (in photons/meter/radian) vs. polar angle (measured around the vacuum chamber, with zero angle corresponding to the radial outside direction), averaged over each type of magnetic environment.

Compared to Example S3, with no diffuse scattering (see Fig. 9), the photon intensity on the top and bottom of the chamber (polar angles of $\pi/2$ and $3\pi/2$) is now much higher, and is comparable to that seen in Example S2. This is due to the out-of-plane diffuse scattering, which results in substantial amounts of radiation scattering out of the median plane. In addition, the radiation striking the radial inside edge of the vacuum chamber (polar angle near π) is also increased.

Example D2: Effect of variation of the diffuse scattering parameters For the second example, photon emission throughout the CESRTA ring from a 2.1 GeV positron beam is simulated again, with a realistic vacuum chamber profile. In this case, the effects of varying the diffuse scattering parameters is illustrated.

In Fig. 16, the photon intensity distribution, averaged over each type of magnetic environment, is shown, for four different cases. The red points correspond to the diffuse scattering parameters $\sigma = 200$ nm and $T = 5500$ nm (same as Fig. 15). The black points correspond to pure specular reflection (same as Fig. 9). Two intermediate cases are also shown: the blue points correspond to still a rough surface, but with $\sigma = 100$ nm, and $T = 5500$ nm; and the cyan points correspond to a polished surface ($\sigma = 4$ nm, with $T = 200$ nm).

It can be seen that there is not much dependence on σ for the two rough surface cases. A polished surface gives considerably less scattering, as expected, but there is still a significant difference between this case and pure specular reflection.

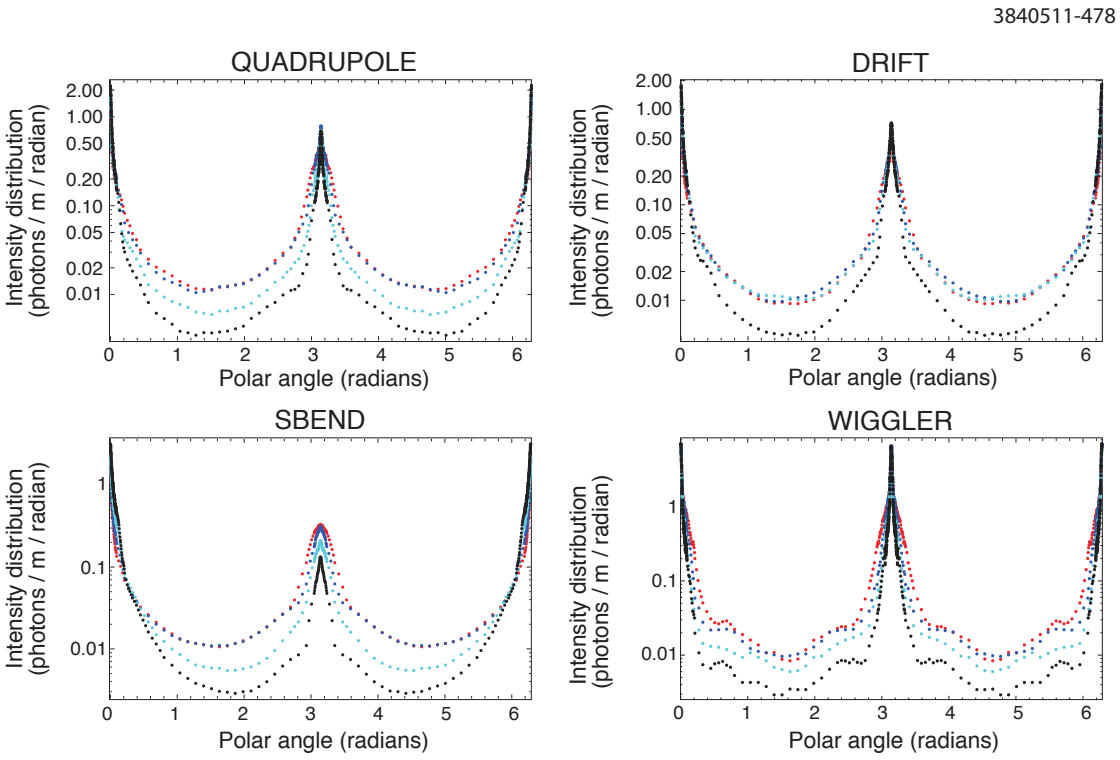

Figure 16: Photon intensity distribution (in photons/meter/radian) vs. polar angle (measured around the vacuum chamber, with zero angle corresponding to the radial outside direction), averaged over each type of magnetic environment. A realistic model for the CESR vacuum chamber throughout the ring is used. The different colors correspond to: red, diffuse scattering parameters $\sigma = 200$ nm and $T = 5500$ nm; blue, diffuse scattering parameters $\sigma = 100$ nm and $T = 5500$ nm; cyan, diffuse scattering parameters $\sigma = 4$ nm and $T = 200$ nm; black, pure specular scattering. Top-bottom symmetry is assumed.

Benchmarking

To provide guidance on the choice of smooth surface reflectivity for a technical aluminum vacuum chamber surface, and to provide an overall check on the scattering model used in `Synrad3D`, we have relied on measurements [11] of X-ray scattering from an aluminum vacuum chamber surface made at DAΦNE. For these measurements, the rms surface roughness of the sample was reported to be 200 nm.

The `Synrad3D` scattering model was used to predict the measured X-ray reflectivity. The autocorrelation parameter T, together with the surface layer thickness and composition (which determine the smooth surface reflectivity, as tabulated in the LBNL X-ray database [5]), were treated as unknowns. (The substrate below the surface layer was assumed to be aluminum). These quantities were adjusted to give the best fit to the measurements.

The best-fit value for the transverse autocorrelation parameter, T, was found to be 5500 nm. The best fit surface layer was found to be a 10 nm carbon layer. The assumption of an aluminum oxide surface layer was not consistent with the data. The data and the corresponding best fits are shown in Fig. 17 and 18.

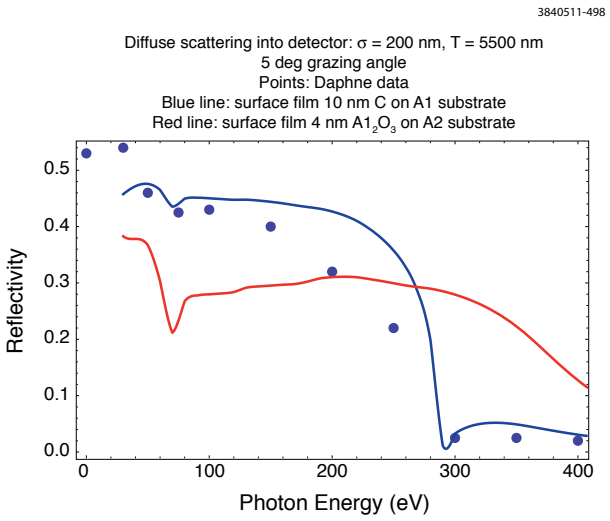

Figure 17: Diffuse scattering at 5 deg from a surface layer on an aluminum substrate: comparison of data [11] and model.

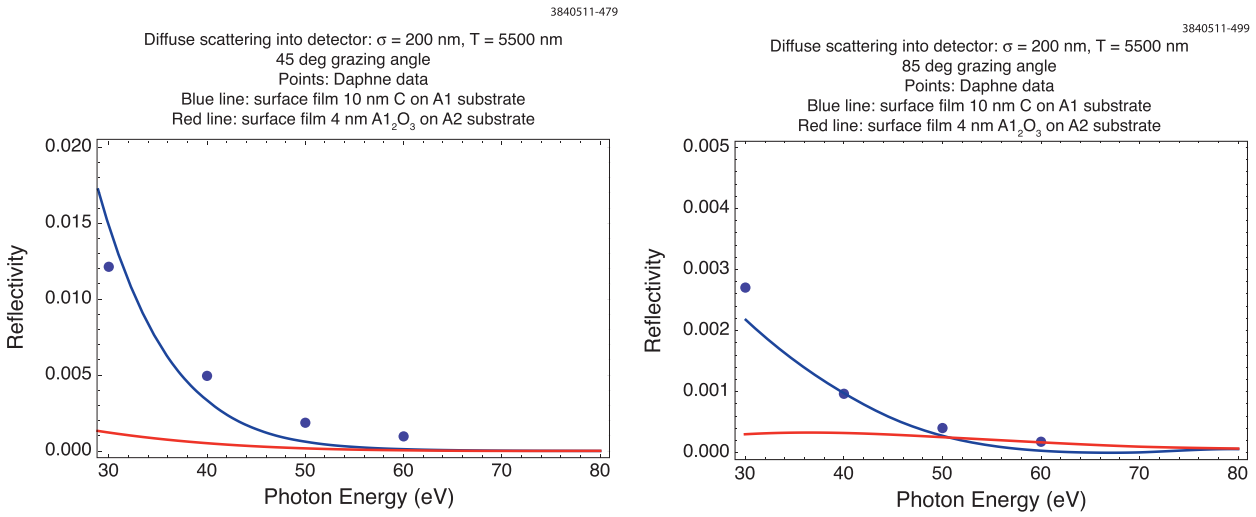

Figure 18: Diffuse scattering a from a surface layer on an aluminum substrate: comparison of data [11] and model. Left: 45°. Right: 85°.

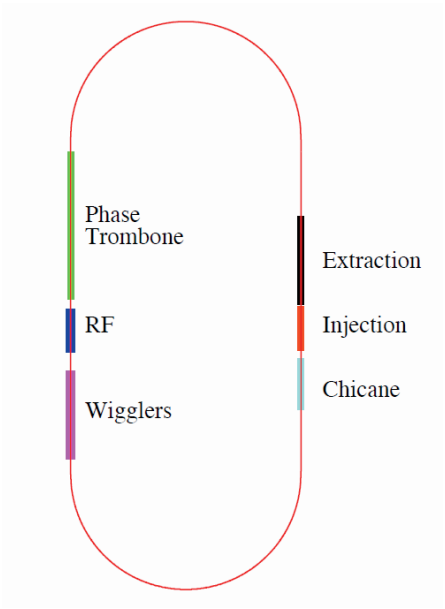

Figure 19: ILC damping ring schematic layout

APPLICATION TO THE ILC DAMPING RING

As part of the effort [12] to characterize the electron cloud effect in the ILC damping ring, `Synrad3D` has been used to predict the radiation environment in the vacuum chamber of the ring. The ring layout is shown in Fig. 19. The radiation environment will be different in the arc regions, where the principal source of photons is the arc dipoles, and the wiggler region, where the wigglers are a source of intense radiation.

Fig. 20 shows the design of the vacuum chamber. The radial inside and outside of the wiggler antechamber are designed to fully absorb any photons which strike them. In the arc and dipole antechambers, a slanted wall on the radial outside reduces the scattering of photons back into the chamber.

The photon distributions predicted by `Synrad3D` are illustrated in Fig. 21. Top-down symmetry is broken here, because of the backscattering from the slanted wall of the arc and dipole antechambers. The absence of photons at zero and π radians are due to the antechambers.

SUMMARY

As part of the Bmad code ecosystem, a program called `Synrad3D` has been written to track synchrotron radiation photons generated in storage rings. It can handle any planar lattice and a wide variety of vacuum chamber profiles.

The program includes scattering from the vacuum chamber walls, based on X-ray data from an LBNL database [5] for the smooth-surface reflectivity, and an analytical model for diffuse scattering from a surface with finite roughness.

The predictions of the scattering model have been benchmarked against measurements at `DAΦNE`. Additional benchmarking against recent X-ray scattering measurements are planned.

Results from the program have given photon absorption site distributions for the CESRTA ring, which have been used as input to electron cloud buildup simulations, whose results can be compared with tune shift [13], RFA, and shielded pickup measurements[14]. The program has also been used to model the radiation environment in the ILC damping ring and the APS[15].

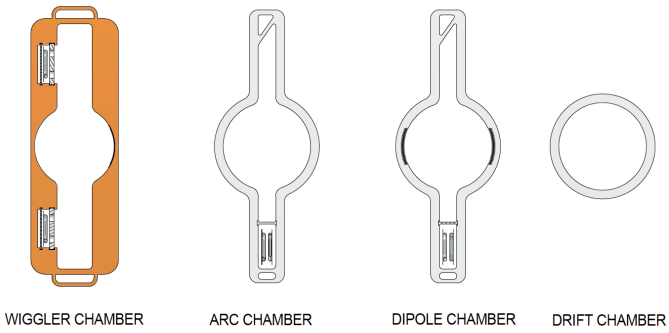

Figure 20: Vacuum chamber designs for magnetic elements in the ILC damping ring. The upper part of the figures correspond to the outer radius of the ring, when installed.

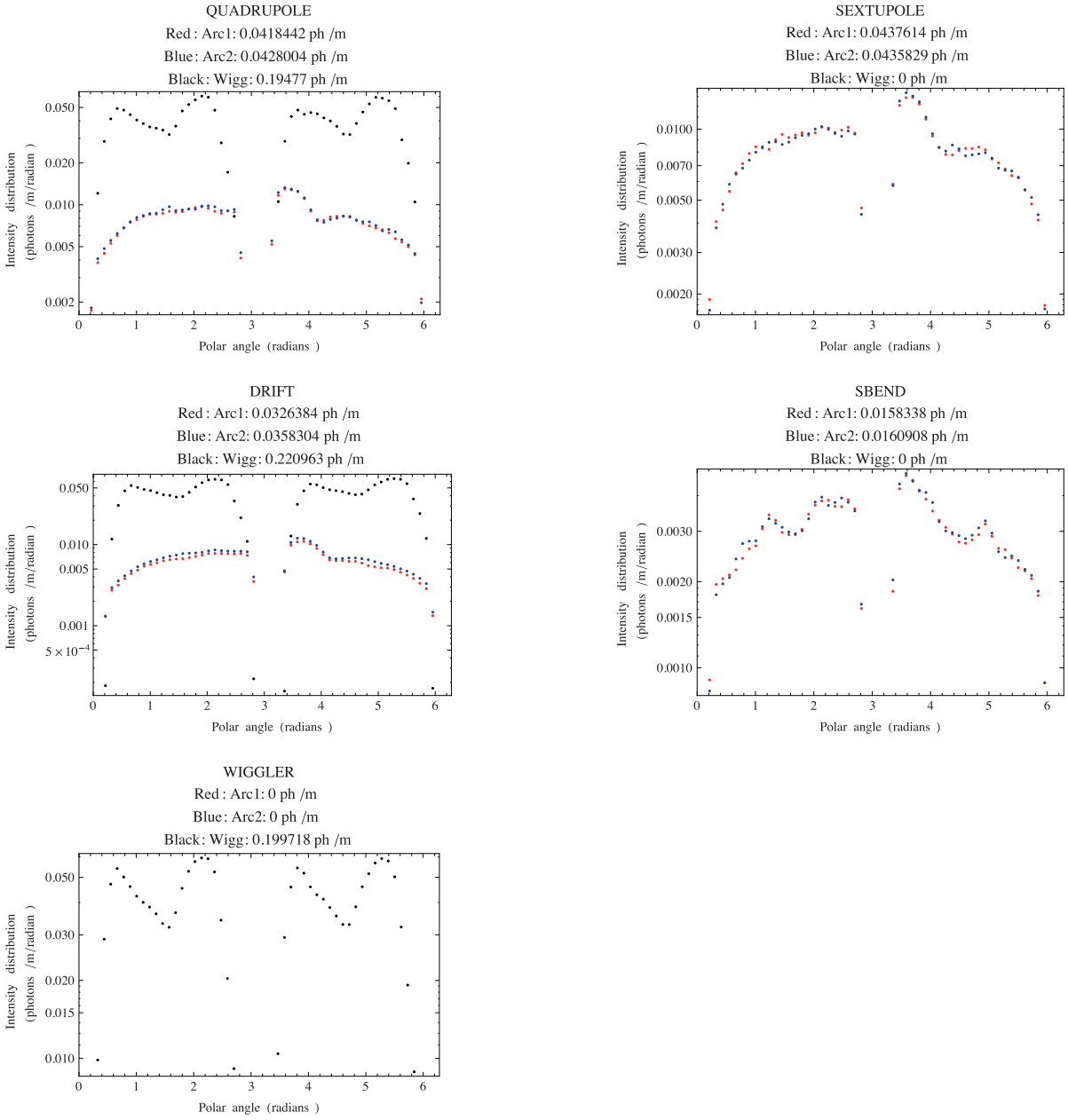

Figure 21: Photon absorption rates in different magnetic environments and ring regions for the ILC damping ring.

REFERENCES

[1] D. Sagan, "Design and Applications of the Bmad Library for the Simulation of Particle Beams and X-rays," in *11th International Computational Accelerator Physics Conference*, Rostock-Warnemünde, Germany (2012).

[2] M. A. Palmer *et al.*, "The Conversion and Operation of the Cornell Electron Storage Ring as a Test Accelerator (CesrTA) for Damping Rings Research and Development'," in *Proceedings of the 2009 Particle Accelerator Conference*, Vancouver, BC (2009), p. 4200–4204.

[3] G. Dugan & D. Sagan, "Synrad3D Photon Propagation and Scattering Simulation," in *Proceedings of ECLOUD 2010: 49th ICFA Advanced Beam Dynamics Workshop on Electron Cloud Physics*, K. Smolenski, Ed., Ithaca, NY (in press), Paper PST08.

[4] G. Dugan & D. Sagan, "SYNRAD3D Photon Tracking Program," Tech. rep., Cornell University (2012), `http://www.lepp.cornell.edu/~dcs16/synrad3d.pdf`.

[5] B. L. Henke, E. M. Gullikson & J. C. Davis, "X-Ray Interactions: Photoabsorption, Scattering, Transmission, and Reflection at E = 50–30,000 eV, Z = 1–92," *At. Data Nucl. Data Tables* **54**, p. 181–342 (Jul. 1993).

[6] P. Beckmann & A. Spizzichino, *The Scattering of Electromagnetic Waves from Rough Surfaces*, Pergamon Press, New York (1963).

[7] J. A. Ogilvy, *Theory of Wave Scattering from Random Rough Surfaces*, Hilger, Bristol (1993).

[8] D. Sagan, "Bmad Manual," Tech. rep., Cornell University (2012), `http://www.lepp.cornell.edu/~dcs16/bmad/`.

[9] H. Hogrefe & C. Kunz, "Soft X-Ray Scattering from Rough Surfaces: Experimental and Theoretical Analysis," *Appl. Opt.* **26**, p. 2851–2859 (Jul. 1987).

[10] R. J. Noll & P. Glenn, "Mirror Surface Autocovariance Functions and their Associated Visible Scattering," *Appl. Opt.* **21**, p. 1824–1838 (May 1982).

[11] N. Mahne *et al.*, "Experimental Determination of e-Cloud Simulation Input Parameters for DAΦNE," Tech. Rep. EUROTEV-REPORT-2005-013, EUROTeV (2005), `http://www.eurotev.org/reports__presentations/eurotev_reports/2005/e371/EUROTeV-Report-2005-013.pdf`.

[12] J. A. Crittenden *et al.*, "Investigation into Electron Cloud Effects in the ILC Damping Ring Design," in *Proceedings of the 2012 International Particle Accelerator Conference*, New Orleans, LA (2012), p. 1963–5.

[13] G. Dugan *et al.*, "Observations and Predictions at CesrTA, and Outlook for ILC," in *Proceedings of ECLOUD'12*, La Biodola, Elba, Italy (2012).

[14] J. A. Crittenden, "Electron Cloud Buildup Characterization Using Shielded Pickup Measurements and Custom Modeling Code," in *Proceedings of ECLOUD'12*, La Biodola, Elba, Italy (2012).

[15] L. Boon, "Chamber Surface Roughness and Electron Cloud for the APS SCU," in *Proceedings of ECLOUD'12*, La Biodola, Elba, Italy (2012).